Spin-polarized electron vortices produced in single-photon ionization

Yibo Hu,[1] Qiangfei Ma,[1] Kunlong Liu ⬤,[1,*] Yidian Tian ⬤,[1] Min Li ⬤,[1] Yueming Zhou,[1,†] and Peixiang Lu[1,2,3]

[1]*Wuhan National Laboratory for Optoelectronics and School of Physics, Huazhong University of Science and Technology, Wuhan 430074, China*
[2]*Hubei Key Laboratory of Optical Information and Pattern Recognition, Wuhan Institute of Technology, Wuhan 430205, China*
[3]*Optics Valley Laboratory, Hubei 430074, China*

We theoretically investigate a scheme to produce spin-polarized electrons based on the vortex interference of the photoelectrons in single-photon ionization. A pair of time-delayed counterrotating circularly polarized pulses are applied to ionize the rare-gas-atom krypton. The results show that the vortex-shaped photoelectron momentum distributions for the ionization channels of $J = 1/2$ and $J = 3/2$, as well as those associated with the initial p_+ and p_- orbitals, can be well dislocated in momentum space, leading to the spin polarization exceeding 50%. Furthermore, by modifying the time delay, the wavelength, and the relative phase of the pulse pair, we show that the kinetic energy as well as the ejection angle of the spin-polarized electrons can be flexibly controlled in the present scheme.

I. INTRODUCTION

Spin is an exploitable degree of freedom of electrons [1]. Since its discovery, spin-polarized electrons have been studied for a wide range of applications, such as exploring the structure of atoms, molecules, and solids [2]; characterizing and probing chiral systems [3,4]; and studying the magnetization profiles in nanostructures [5–7]. Meanwhile, the production of spin-polarized electrons from photoionization has been an important topic for decades. Early in the 1960s, Fano theoretically proposed that in single-photon ionization of a Cs atom in a circularly polarized light, spin polarization of the photoelectrons can be achieved in the vicinity of the Cooper minima due to the effect of spin-orbit interaction [8]. This phenomenon attracted further theoretical [9] and experimental [10,11] interest, and its extension to resonant multiphoton ionization in the weak-field limit was accomplished by Lambropoulos (see Ref. [12] for a review).

A physically different way to produce spin-polarized photoelectrons is the nonadiabatic tunnel ionization of atoms, as proposed by Barth and Smirnova in 2013 [13]. It was predicted [13] and experimentally confirmed [14] that in circularly polarized fields, the spin polarization of photoelectrons arises from the combined effects of spin-orbit interaction and the selective ejection of p-orbital electrons with different magnetic quantum numbers from rare gases. Under such a mechanism, the spin polarization becomes controllable via manipulation of the electronic dynamics with tailored laser fields. For example, it was shown that angle-resolved spin polarization can be achieved by applying attoclock angular streaking [15]. Meanwhile, orthogonal two-color fields [16] and bicircular laser pulses [17] have also been used to control the spin polarization of the photoelectrons. Usually, due to the

fourfold degeneracy of the ionic ground state $P_{3/2}$ of rare-gas atoms, the overall spin polarization of photoelectrons is limited by 50% [13]. In addition to the atomic systems, the diatomic molecule nitric oxide has been shown to be a promising candidate for producing highly spin polarized electrons, enabled by its open-shell orbital structure and the different ionization rates for $\pi_\pm$ orbitals in rotating laser fields [18–20].

In 2018, two research groups independently demonstrated that the above-threshold ionization (ATI) spectra for the ionization channels to the ionic states $J = 1/2$ and $J = 3/2$ of xenon can be well separated in ultraviolet ($\sim$400 nm) laser pulses, resulting in oscillating spin polarization as a function of electronic kinetic energy [21,22]. Particularly, the maximum of the spin polarization could exceed 50% in their studies. Such a scheme requires a particular photon energy that approximately equals twice the ionization potential difference of two ionization channels of xenon; for other atoms, one would need to appropriately tune the pulse frequency so that the spectra for two ionization channels can be separated as desired.

Alternatively, as the ATI peaks are essentially the interference structure originating from the photoelectron ejected at each optical cycle, it would be appealing to seek a more flexible way to steer the photoelectron interference in momentum space and achieve controllable spin polarization. Here, we turn to the scheme based on electron vortices, which appear to be a vortex-shaped interference pattern in the photoelectron momentum distribution (PMD) for photoionization by two time-delayed counterrotating circularly polarized laser pulses [23–30]. The origin of the electron vortices is the interference of two time-delayed electronic wave packets with different magnetic quantum numbers m [31–33]. By analyzing the vortex-shaped momentum distributions, researchers are able to extract the electronic displacement in an ultrashort laser pulse [34], to detect the electronic ring currents associated with different quantum states [35], to extract the phase

---

*liukunlong@hust.edu.cn

†zhouymhust@hust.edu.cn

distributions of the photoelectron wave packets [36], and so on. In the present work, we show that the way to produce electron vortices in single-photon ionization is also a powerful approach for manipulating spin-polarized photoelectrons. The underlying mechanism of our scheme relies on the phase difference between the wave functions of the $p_\pm$ electrons. We show that, as the phase information is encoded in the vortex-shaped momentum distribution, the photoelectrons from the $p_\pm$ orbitals can be separated in momentum space by wave-packet interference. More importantly, the spectra for the ionization channels to the ionic states $J = 1/2$ and $J = 3/2$ are also well separated in the electron vortices. This ultimately leads to spin polarization exceeding 50%. Furthermore, our numerical results show that by adjusting the time delay, the wavelength, or the relative phase of two time-delayed laser pluses, the kinetic energy as well as the ejection angle of the spin-polarized electrons can be flexibly controlled.

II. NUMERICAL METHODS

We numerically solve the two-dimensional time-dependent Schrödinger equation (TDSE) within the single-active-electron approximation. In the Coulomb gauge, the TDSE reads (atomic units are used throughout unless stated otherwise)

$$i\frac{\partial}{\partial t}\psi(\mathbf{r}, t) = \left[\frac{1}{2}[-i\boldsymbol{\nabla} + \mathbf{A}(t)]^2 + V(\mathbf{r})\right]\psi(\mathbf{r}, t), \quad (1)$$

where $\mathbf{r} = (x, y)$ is the two-dimensional coordinate of the electron. We use a soft-core potential,

$$V(\mathbf{r}) = -\frac{1 + 35e^{-0.456\mathbf{r}^2}}{\sqrt{\mathbf{r}^2 + a}}, \quad (2)$$

to represent the core-electron interaction for the Kr atom. Due to the spin-orbit interaction, the removal of the valence electron of Kr would lead to the ion being populated in state $^2P_{3/2}$ or $^2P_{1/2}$, providing two ionization channels with slightly different ionization potentials. To reproduce this energy-splitting effect, we adjust the soft-core parameters $a = 4.002$ and $a = 3.922$ to match the ionization potentials $I_p^{P_{3/2}} = 0.515$ a.u. and $I_p^{P_{1/2}} = 0.539$ a.u., respectively. Similar modeling was also applied in previous studies [14,21], and it was shown that the simulation reproduced the experimental results [14].

To form vortex interference patterns in the photoelectron momentum distributions, two time-delayed counterrotating laser pulses with a right-handed circularly polarized (RCP) pulse preceding a left-handed circularly polarized (LCP) pulse (or, an RLCP pulse pair) are used. The vector potential of the laser pulse within the dipole approximation is given by $\mathbf{A}(t) = A_x(t)\mathbf{e}_x + A_y(t)\mathbf{e}_y$, with

$$A_x(t) = -\frac{E_0}{\omega}f(t)\cos(\omega t + \Phi_1)$$

$$-\frac{E_0}{\omega}f(t - t_d)\cos[\omega(t - t_d) + \Phi_2], \quad (3)$$

$$A_y(t) = \frac{E_0}{\omega}f(t)\sin(\omega t + \Phi_1)$$

$$-\frac{E_0}{\omega}f(t - t_d)\sin[\omega(t - t_d) + \Phi_2], \quad (4)$$
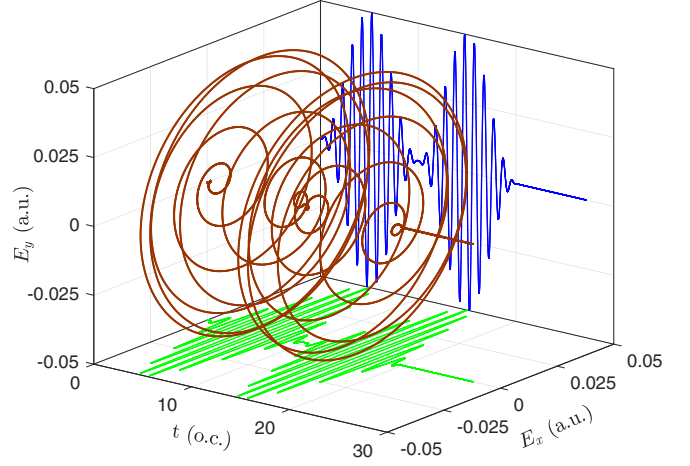
FIG. 1. The electric field $\mathbf{E}(t)$ and its projections on the x and y planes as a function of t. The laser parameters are chosen as $E_0 = 0.05$ a.u., $\omega = 0.7594$ a.u. (corresponding to a wavelength of 60 nm), $t_d = 10$ o.c., $N = 10$, and $\Delta\Phi = 0$.

where E_0, ω, t_d, and Φ_j ($j = 1, 2$) indicate the electric-field amplitude, the laser frequency, the time delay between two pulses, and the carrier-envelope phase (CEP) for the jth pulse, respectively. The relative phase between the two pulses is defined as $\Delta\Phi = \Phi_2 - \Phi_1$. The pulse-envelope function is given by $f(\tau) = \sin^2[\omega\tau/(2N)]$ for $0 \leqslant \tau \leqslant NT$, and otherwise, $f(\tau) = 0$, with $T = 2\pi/\omega$ and N being the optical period and the number of optical cycles (o.c.) of the full pulse, respectively. Figure 1 shows the time evolution of the electric field for the RLCP pulse pair given by $\mathbf{E}(t) = -\partial\mathbf{A}(t)/\partial t$.

The split-operator spectral method [37] on a Cartesian grid is used to numerically solve the two-dimensional TDSE. The Cartesian grid ranges from -120 to 120 a.u. for both directions with grid steps of $\Delta x = \Delta y = 0.12$ a.u. To obtain the initial wave functions of $4p_\pm$ orbitals with $m = \pm 1$, we first calculate the $|\psi_{4p_x}\rangle$ and $|\psi_{4p_y}\rangle$ states by imaginary-time propagation [38] under symmetry conditions. The $|\psi_{4p_\pm}\rangle$ states are given by $|\psi_{4p_\pm}\rangle = (|\psi_{4p_x}\rangle \pm i|\psi_{4p_y}\rangle)/\sqrt{2}$. In real-time propagation, the time step of propagation is chosen as $\delta t = 0.015$ a.u. Every 30 time steps, the electron wave function is smoothly split into the inner and outgoing parts with an absorption function [39]. The inner wave function is propagated under the full Hamiltonian, while the outgoing one representing the ionizing part is analytically propagated under the Volkov Hamiltonian [40]. To calculate the PMD, the outgoing wave function split at each moment is transformed from coordinate space to momentum space, and then it is propagated to the end of the pulse under the Volkov Hamiltonian. By superposing all outgoing wave functions in momentum space at the end of the propagation, we can eventually obtain the PMD for the interaction [41].

III. RESULTS AND DISCUSSION

To obtain the spin polarization of the photoelectrons in the frame of TDSE, let us recall the relationship between the nonrelativistic orbitals p_m ($m = 0, \pm 1$) and the relativistic spin orbitals p_{jm_j}. Here, j and m_j denote the total angular

quantum number and the corresponding magnetic quantum number, respectively. According to [13,17,21], the orbitals p_{jm_j} can be expanded in the basis of the products of orbitals p_m via Clebsch-Gordan coefficients $C^{jm_j}_{lm,sm_s}$ as follows:

$$w^{p_{jm_j}}\left(\mathbf{p}; I_p^{P_j}\right) = \sum_{m,m_s} \left|C^{jm_j}_{1m,\frac{1}{2}m_s}\right|^2 w^{p_m}\left(\mathbf{p}; I_p^{P_j}\right), \qquad (5)$$

where $w(\mathbf{p})$ and $I_p^{P_j}$ represent the PMDs of different orbitals and the ionization potential for the ionization channel that leaves the ion in the ^2P_j state, respectively. Specifically, we have

$$w^{p_{\frac{1}{2}\pm\frac{1}{2}}}\left(\mathbf{p}; I_p^{P_{\frac{1}{2}}}\right) = \tfrac{2}{3} w^{p_\pm}\left(\mathbf{p}; I_p^{P_{\frac{1}{2}}}\right) + \tfrac{1}{3} w^{p_0}\left(\mathbf{p}; I_p^{P_{\frac{1}{2}}}\right), \quad (6)$$

$$w^{p_{\frac{3}{2}\pm\frac{1}{2}}}\left(\mathbf{p}; I_p^{P_{\frac{3}{2}}}\right) = \tfrac{1}{3} w^{p_\pm}\left(\mathbf{p}; I_p^{P_{\frac{3}{2}}}\right) + \tfrac{2}{3} w^{p_0}\left(\mathbf{p}; I_p^{P_{\frac{3}{2}}}\right), \quad (7)$$

$$w^{p_{\frac{3}{2}\pm\frac{3}{2}}}\left(\mathbf{p}; I_p^{P_{\frac{3}{2}}}\right) = w^{p_\pm}\left(\mathbf{p}; I_p^{P_{\frac{3}{2}}}\right). \qquad (8)$$

As the magnetic quantum numbers m and m_s are restricted by $m + m_s = m_j$, the spin-resolved PMD can be calculated by

$$w_{\uparrow,\downarrow}(\mathbf{p}) = w^{p_\pm}\left(\mathbf{p}; I_p^{P_{\frac{3}{2}}}\right) + \tfrac{2}{3} w^{p_\mp}\left(\mathbf{p}; I_p^{P_{\frac{1}{2}}}\right)$$
$$+ \tfrac{1}{3} w^{p_\mp}\left(\mathbf{p}; I_p^{P_{\frac{3}{2}}}\right), \qquad (9)$$

where $w_\uparrow(\mathbf{p})$ [$w_\downarrow(\mathbf{p})$] is the PMD for the spin-up (spin-down) orbitals. The contribution from the p_0 orbital is omitted in Eq. (9) since the ionization for $m = 0$ is significantly suppressed. Then, the spin polarization is finally expressed as

$$\chi(\mathbf{p}) = \frac{w_\uparrow(\mathbf{p}) - w_\downarrow(\mathbf{p})}{w_\uparrow(\mathbf{p}) + w_\downarrow(\mathbf{p})}$$

$$= \frac{2}{3} \frac{w^{p_+}\left(\mathbf{p}; I_p^{P_{\frac{3}{2}}}\right) - w^{p_-}\left(\mathbf{p}; I_p^{P_{\frac{3}{2}}}\right)}{w_{all}(\mathbf{p})}$$

$$+ \frac{2}{3} \frac{w^{p_-}\left(\mathbf{p}; I_p^{P_{\frac{1}{2}}}\right) - w^{p_+}\left(\mathbf{p}; I_p^{P_{\frac{1}{2}}}\right)}{w_{all}(\mathbf{p})}$$

$$= \frac{2}{3} \frac{w^{p_+}\left(\mathbf{p}; I_p^{P_{\frac{3}{2}}}\right) - w^{p_+}\left(\mathbf{p}; I_p^{P_{\frac{1}{2}}}\right)}{w_{all}(\mathbf{p})}$$

$$+ \frac{2}{3} \frac{w^{p_-}\left(\mathbf{p}; I_p^{P_{\frac{1}{2}}}\right) - w^{p_-}\left(\mathbf{p}; I_p^{P_{\frac{3}{2}}}\right)}{w_{all}(\mathbf{p})}. \qquad (10)$$

From Eq. (10), one can see that the momentum-resolved spin polarization of the photoelectrons depends on two aspects: (i) the contrast between the PMDs for the p_+ and p_- orbitals under the same ionization potential and (ii) the contrast between the PMDs for the p_+ (and p_-) orbital under two ionization potentials. In the following discussion, we will see that the electron vortices produced by the counterrotating pulse pair fulfill both conditions.

In Fig. 2, we demonstrate the PMDs for four $p_m(I_p^{P_j})$ orbitals of the Kr atom ionized by the RLCP pulse pair illustrated in Fig. 1. In general, all the four PMDs show the vortex structures, and the number of spiral arms is two. On the one hand, by comparing the PMDs for the orbitals possessing the same angular momentum but different ionization potentials, i.e., $p_+(I_p^{P_{\frac{3}{2}}})$ vs $p_+(I_p^{P_{\frac{1}{2}}})$ [Figs. 2(a) and 2(c)] and $p_-(I_p^{P_{\frac{3}{2}}})$ vs
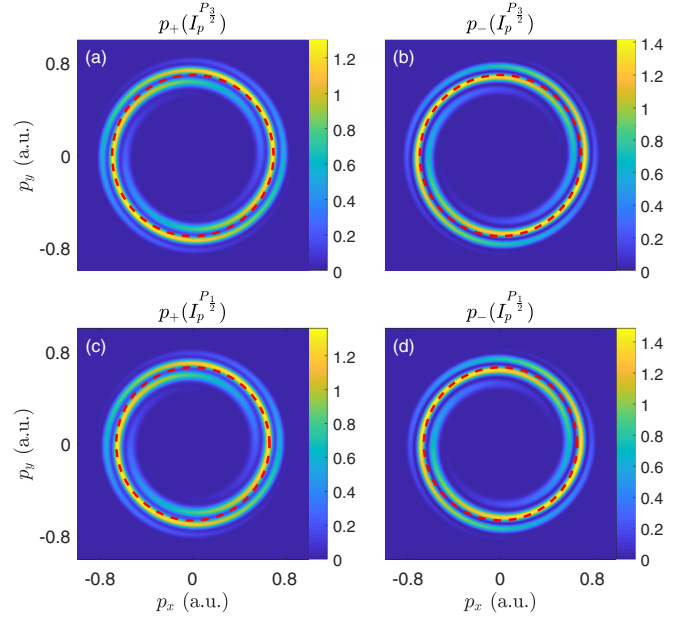
FIG. 2. The PMDs for four $p_m(I_p^{P_j})$ orbitals of the Kr atom ionized by the RLCP pulse pair. The parameters of the RLCP pulse pair are the same as in Fig. 1. The dashed red rings indicate the momentum at $p_r = \sqrt{2(\omega - I_p^{P_j})}$.

$p_-(I_p^{P_{\frac{1}{2}}})$ [Figs. 2(b) and 2(d)], one can see that the electron vortices for the $p(I_p^{P_{\frac{1}{2}}})$ orbitals are generally distributed at a relatively smaller momentum compared with the $p(I_p^{P_{\frac{3}{2}}})$ orbitals due to their deeper ionization potential and thus lower kinetic energy. On the other hand, by comparing the PMDs for the orbitals with the same ionization potential but different angular momenta, i.e., $p_+(I_p^{P_{\frac{3}{2}}})$ vs $p_-(I_p^{P_{\frac{3}{2}}})$ [Figs. 2(a) and 2(b)] and $p_+(I_p^{P_{\frac{1}{2}}})$ vs $p_-(I_p^{P_{\frac{1}{2}}})$ [Figs. 2(c) and 2(d)], we find a rotational offset between the vortex structures for the p_+ and p_- orbitals.

The vortex-shaped interference patterns on the PMDs in Fig. 2 can be explained by the coherent superposition of two time-delayed photoelectron wave packets with different magnetic quantum numbers m. When the photoelectrons are released separately by two time-delayed counterrotating laser pulses, the superimposed wave packets of the photoelectrons from the $p_\pm$ orbitals can be expressed as [32,42]

$$\Psi_\pm(\phi, K) = \sum_{j=1,2} M_j(\phi, K) e^{i[m_j(\phi+\Delta\phi_\pm)-K(t-t_j)+\Phi_j]},$$
$$(11)$$

where ϕ is the angle between the photoelectron momentum direction and the horizontal axis on the polarization plane; $K = \mathbf{p}^2/2$ is the kinetic energy of the photoelectron; and $M_j(\phi, K)$, m_j, and t_j are the amplitude, the angular quantum number, and the time when the photoelectron wave packet is generated, respectively. The subscript j indicates the quantity for the jth pulse. Note that the global phase Φ_j introduced by the CEP has been taken into account. $\Delta\phi_\pm$ represents the overall angular rotation of the wave function due to the
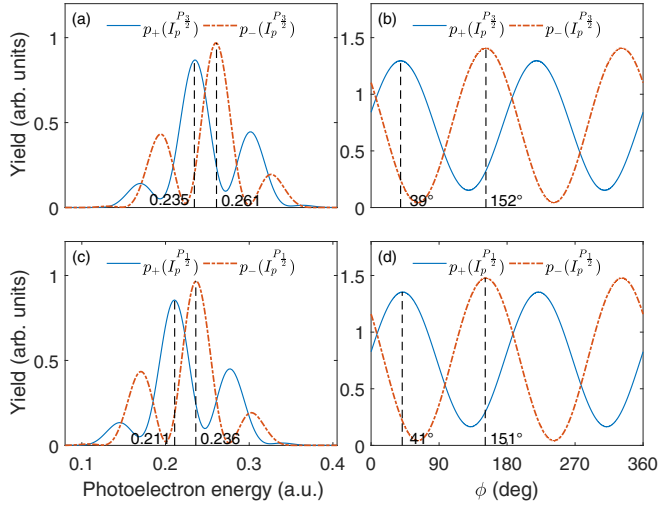
FIG. 3. (a) and (c) PEDs in the direction of $\phi = 0$ and (b) and (d) PADs cut at $p_r = \sqrt{2(\omega - I_p^{P_j})}$ for different $p_m(I_p^{P_j})$ orbitals. The black dashed lines and numbers indicate the locations of the peaks.

FIG. 4. The momentum-resolved spin polarization $\chi(\mathbf{p})$ of the photoelectrons produced by (a) the RLCP pulse pair, (b) RRCP pulse pair, (c) RCP pulse, and (d) LCP pulse.

nonadiabatic interactions between the rotating pulses and the $p_\pm$ orbitals with opposite nonzero angular momenta. The interference distribution contributed by these two photoelectron wave functions is thus written as

$$|\Psi_\pm(\phi, K)|^2 = |M_1|^2 + |M_2|^2 + 2M_1 M_2$$
$$\times \cos[\Delta m(\phi + \Delta\phi_\pm) - K\Delta t + \Delta\Phi], \quad (12)$$

with $\Delta m = m_2 - m_1$, $\Delta t = t_2 - t_1$, and $\Delta\Phi = \Phi_2 - \Phi_1$. For the single-photon ionization under the RLCP pulse pair in the present case, we have $\Delta m = -2$ [24]. Thus, the two-arm electron vortices in Fig. 2 satisfy the c_{2n} rotational symmetry, which is consistent with previous studies [29–33]. In addition, since the photoelectron will most likely be released at the maximum of the electric field, Δt is related to the time delay t_d between the two pulses. Furthermore, the nonzero quantity $\Delta\phi_\pm$ related to the initial orbitals in Eq. (12) means that the overall interference patterns will be rotated differently for p_+ and p_- orbitals. This explains the rotational offset we found in Fig. 2.

To show quantitatively the differences among the PMDs illustrated in Fig. 2, we calculate the photoelectron energy distributions (PEDs) in the direction of $\phi = 0$, as well as the photoelectron angular distributions (PADs), for four different $p_m(I_p^{P_j})$ orbitals. Figures 3(a) and 3(c) show the PEDs calculated from the initial $p(I_p^{P_{\frac{3}{2}}})$ orbital and $p(I_p^{P_{\frac{1}{2}}})$ orbital, respectively. Instead of a Gaussian-like distribution, the PEDs are modulated and exhibit peaks and valleys because of the wave-packet interference. In particular, due to the deeper ionization potential for $J = 1/2$, the $p(I_p^{P_{\frac{1}{2}}})$-orbital electrons dominate at a relatively lower kinetic energy compared with the $p(I_p^{P_{\frac{3}{2}}})$-orbital electrons. Meanwhile, for a given J, we can see the PED peaks for p_+ and p_- orbitals are dislocated. As indicated by the vertical dashed lines in Figs. 3(a) and 3(c), there is an energy separation of around 0.025 a.u. between the PED peaks for the p_+ and p_- orbitals.
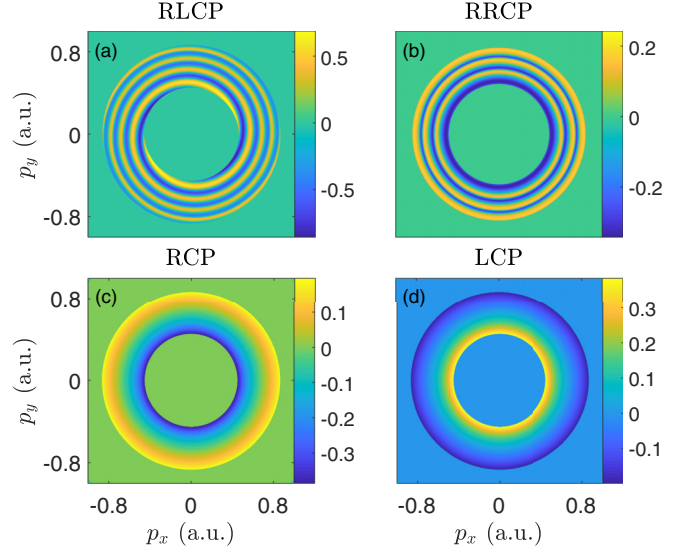
In Figs. 3(b) and 3(d), we illustrate the PADs which are cut at the momentum radius given by $p_r = \sqrt{2(\omega - I_p^{P_j})}$ (marked as red dashed rings in Fig. 2). The PADs appear as a cosinelike oscillating curve with a period of π due to the c_2 rotational symmetry. As indicated by the vertical dashed lines, there is a phase shift of about $110°$ between the PADs for the p_+ and p_- orbitals, while there is insignificant difference between the PADs for the ionization channels of $J = 1/2$ and $J = 3/2$.

So far, we have shown that the photoelectron spectra for the ionization channels of $J = 1/2$ and $J = 3/2$, as well as the p_+ and p_- photoelectrons, can be well separated via the vortex interference in the RLCP pulse pair. Next, let us recall the physical mechanism responsible for producing spin-polarized electrons from rare-gas atoms [13]. Suppose we have created the ion in the $P_{1/2}$ state, which is twofold degenerate: the electron removed from the p_- (p_+) orbital will end up with spin up (down) due to the interplay of electron-ion entanglement. Thus, the separation of the p_+ and p_- photoelectrons would lead to possibly 100% spin polarization in the ionization channel of $J = 1/2$. The case for the channel with $J = 3/2$ is similar, but the upper limit of spin polarization is 50% due to the fourfold-degenerate ion state. Therefore, the ability to separate the p_+ and p_- photoelectrons *and* the photoelectron spectra corresponding to the ionization channels into $P_{3/2}$ and $P_{1/2}$ states will be the key to achieving a high degree of spin polarization of coherent electron beams.

In the following, we calculate the momentum distributions for the spin-up and spin-down photoelectrons according to Eq. (9), and the momentum-resolved distribution of spin polarization $\chi(\mathbf{p})$ is shown in Fig. 4. Note that, for better visibility, $\chi(\mathbf{p})$ has been set to zero when the total yield distribution $[w_\uparrow(\mathbf{p}) + w_\downarrow(\mathbf{p})]$ is too low, specifically lower than 0.58% of the maximum value of the yield distribution. Figure 4(a) demonstrates the momentum-resolved $\chi(\mathbf{p})$ of photoelectrons produced by the RLCP pulse pair. One can see that the distribution of $\chi(\mathbf{p})$ also shows a vortex like
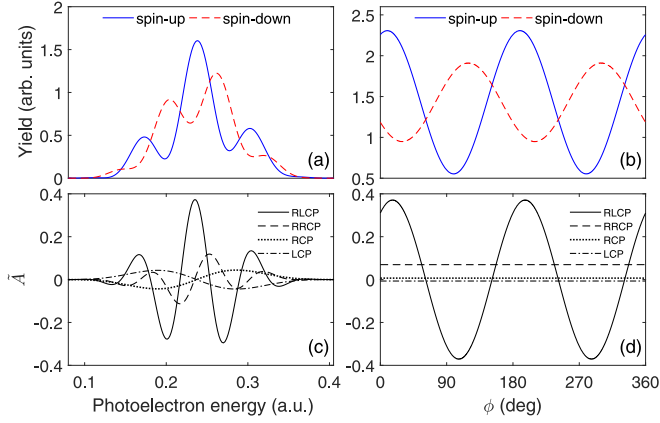
FIG. 5. (a) The energy distribution at $\phi = 0$ and (b) the angular distribution at $p_r = 0.7$ a.u. of spin-up and spin-down electrons produced by the RLCP pulse pair; the solid curves in (c) and (d) are the corresponding distributions of $\tilde{A}$. The dashed, dotted, and dash-dotted curves in (c) and (d) are the distributions of $\tilde{A}$ in the ionization of the RRCP pulse pair, only the RCP pulse, and only the LCP pulse, respectively.

pattern in the RLCP pulse pair, indicating that both energy- and angle-resolved spin polarization can be achieved. The value of $\chi(\mathbf{p})$ ranges between -0.86 and 0.69, which already exceeds 50% spin polarization even though both ionization channels with $J = 1/2$ and $J = 3/2$ have been integrated. Meanwhile, we show in Fig. 4(b) the momentum-resolved $\chi(\mathbf{p})$ of photoelectrons produced by the corotating pulse pair, which is a right-handed circularly polarized pulse preceding a right-handed circularly polarized pulse (RRCP). In this case, although the spin polarization can be achieved as well, $\chi(\mathbf{p})$ oscillates only in the radial direction, and the degree of spin polarization is lower than that in the RLCP pulse pair. In addition, under a single LCP or RCP pulse, there is no interference structure for $\chi(\mathbf{p})$, and the degree of spin polarization is also relatively lower, as shown in Figs. 4(c) and 4(d).

Furthermore, we show the energy spectra at $\phi = 0$ and the angular distributions at $p_r = 0.7$ a.u. of the spin-up and spin-down photoelectrons produced by the RLCP pulse pair in Figs. 5(a) and 5(b), respectively, where we can see that the spectrum peaks for spin-up and spin-down electrons are well separated. Correspondingly, we evaluate the yield asymmetry for the spin-up and spin-down electrons using the normalized yield asymmetry parameter [17,21]

$$\tilde{A}(\mathbf{p}) = \frac{w_\uparrow(\mathbf{p}) - w_\downarrow(\mathbf{p})}{\max[w_\uparrow(\mathbf{p}) + w_\downarrow(\mathbf{p})]}. \tag{13}$$

This parameter can give us an impression not only of the asymmetry between the spin-up and spin-down electrons but also of the yield of the spin-polarized electrons. The asymmetry $\tilde{A}$ as a function of the kinetic energy and the emission angle of the photoelectrons is shown in Figs. 5(c) and 5(d), respectively. The solid curves represent the case using the RLCP pulse pair. Significant oscillation of the spin asymmetry can be seen with the variation of the kinetic energy and the emission angle. In contrast, the asymmetry parameter in the case of only one single RCP (dotted curves) or LCP
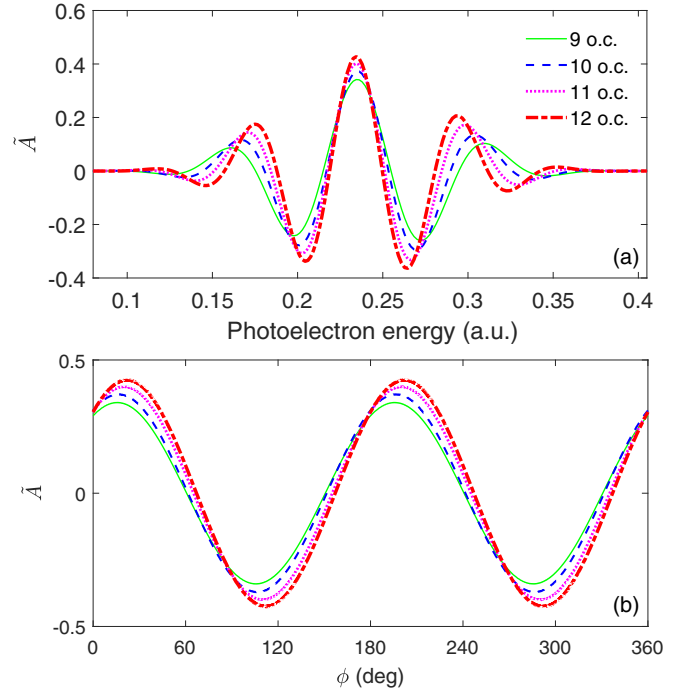
FIG. 6. (a) The energy distribution at $\phi = 0$ and (b) the angular distribution at $p_r = 0.7$ a.u. of $\tilde{A}$ for different time delays t_d; the other parameters of the RLCP pulse pair are the same as in Fig. 1.

(dash-dotted curves) pulse is much less pronounced. This indicates that each pulse of the RLCP pulse pair is not able to achieve significant spin polarization but the vortex interference between the electronic wave packets created by two time-delayed counterrotating pulses will "squeeze" spin-up and spin-down electronic wave packets at a certain kinetic energy and emission angle, leading to the significant and oscillating spin polarization in the spectra. For comparison, we also illustrate the results under the RRCP pulse pair with dashed curves in Figs. 5(c) and 5(d). They show that although $\tilde{A}$ oscillates with the photoelectron energy under the RRCP pulse pair as well, the oscillation amplitude is much smaller than that under the RLCP pulse pair. This is because the PMDs of p_+ and p_- orbitals with the same ionization potential are not well separated under the corotating pulse pair. Note that spin polarization relies on the yield difference in the PMDs of p_+ and p_- orbitals [see Eq. (10)]. On the other hand, we also see that the spin asymmetries $\tilde{A}$ for RRCP are identical at different angles, as two time-delayed photoelectron wave packets carry the same angular momentum in the corotating pulse pair and thus the interference along the angular distribution vanishes.

As analyzed above using Eq. (12), the nonadiabaticity-induced phase difference between $p_\pm$ orbitals plays the key role in squeezing the spin-polarized electronic wave packets. Meanwhile, we can also see that the interference term given in Eq. (12) depends on the photoelectron kinetic energy as well as the time delay between two pulses. Therefore, we further investigate the dependence of the energy- and angle-resolved spin asymmetry $\tilde{A}$ on the laser parameters of the RLCP pulse pair.
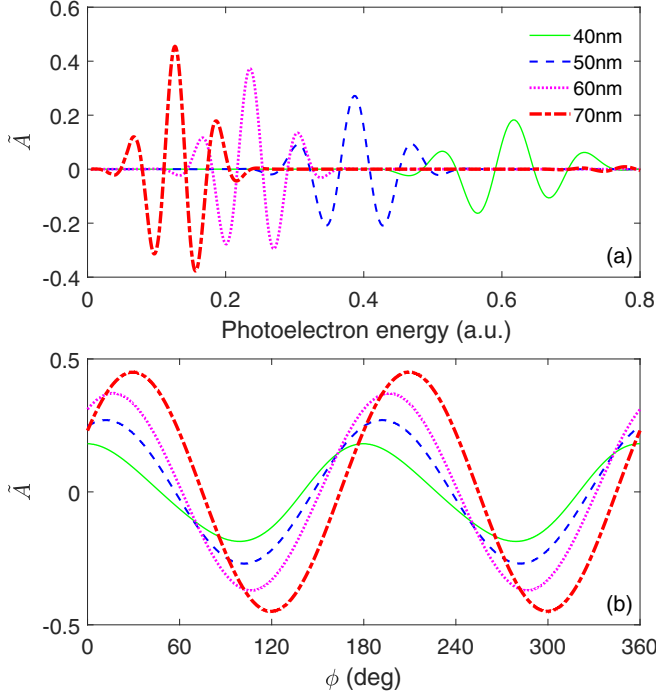
FIG. 7. (a) The energy distribution in the $\phi = 0$ direction and (b) the angular distribution at p_r of $\tilde{A}$ for different laser wavelengths; the other parameters of the RLCP pulse pair are the same as in Fig. 1. Note that for laser wavelengths of 40, 50, 60, and 70 nm, $p_r = 1.1$, 0.9, 0.7, and 0.5 a.u., respectively, where the yield of $[w_\uparrow(p_r) + w_\downarrow(p_r)]$ reaches the maximum.

FIG. 8. (a) The energy distribution in the $\phi = 0$ direction and (b) the angular distribution at $p_r = 0.7$ a.u. of $\tilde{A}$ for different relative phases $\Delta\Phi$; the other parameters of the RLCP pulse pair are the same as in Fig. 1.

First, Fig. 6(a) illustrates the energy distribution of $\tilde{A}$ at different time delays t_d. It can be seen that the interval between the peaks of each curve of $\tilde{A}$ decreases with increasing t_d. This is because the energetic separation of adjacent vortex arms is given by $\delta K = 2\pi/\Delta t$, according to Eq. (12). When t_d increases, there will be more interference maxima in the energy spectrum of the photoelectron, leading to a higher oscillating frequency of $\tilde{A}$, as shown in Fig. 6(a). For the angular distributions, Fig. 6(b) illustrates that $\tilde{A}$ is modified by t_d insignificantly, as the angular distribution at a given kinetic energy is not directly associated with t_d.

Second, the dependence of $\tilde{A}$ on the laser wavelength is illustrated in Fig. 7. The photoelectrons tend to gain less kinetic energy as the wavelength increases. Since we have set $t_d = 10$ o.c., the longer wavelength indicates a larger time delay, which, as discussed above, leads to the higher oscillation frequency of the asymmetry $\tilde{A}$ for longer wavelengths [Fig. 7(a)]. Both Figs. 6(a) and 7(a) show that the squeezing of the spin-up and spin-down electrons in the spectra leads to a relatively higher spin asymmetry as the time delay increases to some extent. In addition, as demonstrated in Fig. 7(b), when the wavelength increases, the angular distribution of $\tilde{A}$ is shifted, and the oscillation amplitude of $\tilde{A}$ also increases.

Finally, considering that the vortex-shaped interference patterns originate from the phase difference between the time-delayed photoelectron wave functions, the CEPs of two laser pulses are expected to have an impact on the vortex structures

and thus the spin polarization. Figure 8 shows the distributions of $\tilde{A}$ for varying $\Delta\Phi$. It is clear that the modulation of the energy and angular distributions of $\tilde{A}$ can be modified by changing the relative phase between two pulses. The varying modulation shown in Fig. 8 indicates that we will be able to adjust the kinetic energy of the spin-polarized electrons to some extent and control their ejection angles by tuning the CEPs of the pulses.

From Figs. 6–8, one can see that the present scheme to produce spin-polarized electrons via the vortex-shaped interference patterns is valid over a certain range of laser conditions. More importantly, the distributions of the spin-polarized electrons on the kinetic energy and the ejection angle can be flexibly controlled by modifying the time delay, the wavelength, or the relative phase of the RLCP pulse pair.

IV. CONCLUSION

In conclusion, due to the energy splitting between the ionization channels with $J = 1/2$ and $J = 3/2$ together with the phase difference between the photoelectron wave packets from the p_+ and p_- orbitals, the vortex-shaped photoelectron momentum distributions for different p_m^J orbitals are well separated in the RLCP pulse pair. The dislocation of the spin-up and spin-down photoelectrons in the momentum space leads to momentum-resolved spin polarization, which exceeds 50% in the present scheme. Additionally, we also show that the kinetic energy and the ejection angle of the spin-polarized electrons can be flexibly controlled by modifying the time

delay, the wavelength, or the relative phase of the RLCP pulse pair. Although the single-photon ionization process was considered in the present study, it is expected that the underlying mechanism will hold for the few-photon ionization as well. Meanwhile, as the shape of the vortex interference can be modified by changing the pulse parameters, our scheme will work not only for krypton but also for other noble-gas atoms and molecules carrying valence electrons with nonzero angular momenta.

[1] G. E. Uhlenbeck and S. Goudsmit, Spinning electrons and the structure of spectra, Nature (London) **117**, 264 (1926).

[2] J. Kessler, *Polarized Electrons* (Springer, Berlin, 1985).

[3] G. Chen, J. Zhu, A. Quesada, J. Li, A. T. N'Diaye, Y. Huo, T. P. Ma, Y. Chen, H. Y. Kwon, C. Won, Z. Q. Qiu, A. K. Schmid, and Y. Z. Wu, Novel Chiral Magnetic Domain Wall Structure in Fe/Ni/Cu(001) Films, Phys. Rev. Lett. **110**, 177204 (2013).

[4] S.-H. Yang, R. Naaman, Y. Paltiel, and S. S. Parkin, Chiral spintronics, Nat. Rev. Phys. **3**, 328 (2021).

[5] H. F. Ding, A. K. Schmid, D. Li, K. Y. Guslienko, and S. D. Bader, Magnetic Bistability of Co Nanodots, Phys. Rev. Lett. **94**, 157202 (2005).

[6] R. Zdyb, A. Pavlovska, M. Jalochowski, and E. Bauer, Self-organized Fe nanostructures on W(1 1 0), Surf. Sci. **600**, 1586 (2006).

[7] Y. R. Niu, K. L. Man, A. Pavlovska, E. Bauer, and M. S. Altman, Fe on W(001) from continuous films to nanoparticles: Growth and magnetic domain structure, Phys. Rev. B **95**, 064404 (2017).

[8] U. Fano, Spin orientation of photoelectrons ejected by circularly polarized light, Phys. Rev. **178**, 131 (1969).

[9] N. A. Cherepkov, Angular distribution and spin orientation of photoelectrons ejected by circularly polarized light, Phys. Lett. A **40**, 119 (1972).

[10] G. Baum, M. S. Lubell, and W. Raith, Spin-Orbit Perturbation in Heavy Alkali Atoms, Phys. Rev. Lett. **25**, 267 (1970).

[11] U. Heinzmann, J. Kessler, and J. Lorenz, Wavelength Dependence of the Fano Effect, Phys. Rev. Lett. **25**, 1325 (1970).

[12] U. Heinzmann and J. H. Dil, Spin-orbit-induced photoelectron spin polarization in angle-resolved photoemission from both atomic and condensed matter targets, J. Phys.: Condens. Matter **24**, 173001 (2012).

[13] I. Barth and O. Smirnova, Spin-polarized electrons produced by strong-field ionization, Phys. Rev. A **88**, 013401 (2013).

[14] A. Hartung, F. Morales, M. Kunitski, K. Henrichs, A. Laucke, M. Richter, T. Jahnke, A. Kalinin, M. Schöffler, L. P. H. Schmidt, M. Ivanov, O. Smirnova, and R. Dörner, Electron spin polarization in strong-field ionization of xenon atoms, Nat. Photonics **10**, 526 (2016).

[15] G. S. J. Armstrong, D. D. A. Clarke, J. Benda, J. Wragg, A. C. Brown, and H. W. van der Hart, Enhancing spin polarization using ultrafast angular streaking, Phys. Rev. A **103**, 053123 (2021).

[16] M. Han, P. Ge, M.-M. Liu, Q. Gong, and Y. Liu, Spatially and temporally controlling electron spin polarization in strong-filed ionization using orthogonal two-color laser fields, Phys. Rev. A **99**, 023404 (2019).

[17] D. B. Milošević, Possibility of introducing spin into attoscience with spin-polarized electrons produced by a bichromatic circularly polarized laser field, Phys. Rev. A **93**, 051402(R) (2016).

[18] K. Liu and I. Barth, Nonadiabatic tunnel ionization of current-carrying orbitals of prealigned linear molecules in strong circularly polarized laser fields, Phys. Rev. A **94**, 043402 (2016).

[19] K. Liu and I. Barth, Spin-polarized photoelectrons produced by strong-field ionization of randomly aligned nitric oxide, J. Mod. Opt. **64**, 987 (2017).

[20] K. Liu, K. Renziehausen, and I. Barth, Producing spin-polarized photoelectrons by using the momentum gate in strong-field ionization experiments, Phys. Rev. A **95**, 063410 (2017).

[21] M.-M. Liu, Y. Shao, M. Han, P. Ge, Y. Deng, C. Wu, Q. Gong, and Y. Liu, Energy- and Momentum-Resolved Photoelectron Spin Polarization in Multiphoton Ionization of Xe by Circularly Polarized Fields, Phys. Rev. Lett. **120**, 043201 (2018).

[22] D. Trabert, A. Hartung, S. Eckart, F. Trinter, A. Kalinin, M. Schöffler, L. Ph. H. Schmidt, T. Jahnke, M. Kunitski, and R. Dörner, Spin and Angular Momentum in Strong-Field Ionization, Phys. Rev. Lett. **120**, 043202 (2018).

[23] J. M. Ngoko Djiokap, S. X. Hu, L. B. Madsen, N. L. Manakov, A. V. Meremianin, and A. F. Starace, Electron Vortices in Photoionization by Circularly Polarized Attosecond Pulses, Phys. Rev. Lett. **115**, 113004 (2015).

[24] D. Pengel, S. Kerbstadt, D. Johannmeyer, L. Englert, T. Bayer, and M. Wollenhaupt, Electron Vortices in Femtosecond Multiphoton Ionization, Phys. Rev. Lett. **118**, 053003 (2017).

[25] M. Li, G. Zhang, X. Kong, T. Wang, X. Ding, and J. Yao, Dynamic stark induced vortex momentum of hydrogen in circular fields, Opt. Express **26**, 878 (2018).

[26] K. Eickhoff, L. Englert, T. Bayer, and M. Wollenhaupt, Multichromatic polarization-controlled pulse sequences for coherent control of multiphoton ionization, Front. Phys. **9**, 675258 (2021).

[27] K.-J. Yuan, S. Chelkowski, and A. D. Bandrauk, Photoelectron momentum distributions of molecules in bichromatic circularly polarized attosecond UV laser fields, Phys. Rev. A **93**, 053425 (2016).

[28] J. M. Ngoko Djiokap, A. V. Meremianin, N. L. Manakov, L. B. Madsen, S. X. Hu, and A. F. Starace, Dynamical electron vortices in attosecond double photoionization of H_2, Phys. Rev. A **98**, 063407 (2018).

[29] L. Geng, F. Cajiao Vélez, J. Z. Kamiński, L.-Y. Peng, and K. Krajewska, Structured photoelectron distributions in photodetachment induced by trains of laser pulses: Vortices versus spirals, Phys. Rev. A **104**, 033111 (2021).

[30] M.-Y. Ma, J.-P. Wang, W.-Q. Jing, Z. Guan, Z.-H. Jiao, G.-L. Wang, J.-H. Chen, and S.-F. Zhao, Controlling the atomic-orbital-resolved photoionization for neon atoms by counter-rotating circularly polarized attosecond pulses, Opt. Express **29**, 33245 (2021).

[31] J. M. Ngoko Djiokap, A. V. Meremianin, N. L. Manakov, S. X. Hu, L. B. Madsen, and A. F. Starace, Multistart spiral electron vortices in ionization by circularly polarized UV pulses, Phys. Rev. A **94**, 013408 (2016).

[32] D. Pengel, S. Kerbstadt, L. Englert, T. Bayer, and M. Wollenhaupt, Control of three-dimensional electron vortices from femtosecond multiphoton ionization, Phys. Rev. A **96**, 043426 (2017).

[33] J. M. N. Djiokap and A. F. Starace, Doubly-excited state effects on two-photon double ionization of helium by time-delayed, oppositely circularly-polarized attosecond pulses, J. Opt. **19**, 124003 (2017).

[34] X.-R. Xiao, M.-X. Wang, H. Liang, Q. Gong, and L.-Y. Peng, Proposal for Measuring Electron Displacement Induced by a Short Laser Pulse, Phys. Rev. Lett. **122**, 053201 (2019).

[35] R. Wang, Q. Zhang, C. Ran, W. Cao, and P. Lu, Proposal for detecting ring current via electron vortices, Opt. Lett. **45**, 1383 (2020).

[36] Y. Qin, M. Li, Y. Feng, S. Luo, Y. Zhou, and P. Lu, Extracting the phase distribution of the electron wave packet ionized by an elliptically polarized laser pulse, Front. Phys. **16**, 32502 (2021).

[37] M. D. Feit, Jr., J. A. Fleck, Jr., and A. Steiger, Solution of the Schrödinger equation by a spectral method, J. Comput. Phys. **47**, 412 (1982).

[38] M. Protopapas, C. H. Keitel, and P. L. Knight, Atomic physics with super-high intensity lasers, Rep. Prog. Phys. **60**, 389 (1997).

[39] S. Chelkowski, C. Foisy, and A. D. Bandrauk, Electron-nuclear dynamics of multiphoton H_2^+ dissociative ionization in intense laser fields, Phys. Rev. A **57**, 1176 (1998).

[40] X. M. Tong, K. Hino, and N. Toshima, Phase-dependent atomic ionization in few-cycle intense laser fields, Phys. Rev. A **74**, 031405 (2006).

[41] Y. Fu, J. Zeng, and J. Yuan, PCTDSE: A parallel Cartesian-grid-based TDSE solver for modeling laser-atom interactions, Comput. Phys. Commun. **210**, 181 (2017).

[42] K. Liu, H. Ni, K. Renziehausen, J.-M. Rost, and I. Barth, Deformation of Atomic $p_{\pm}$ Orbitals in Strong Elliptically Polarized Laser Fields: Ionization Time Drifts and Spatial Photoelectron Separation, Phys. Rev. Lett. **121**, 203201 (2018).